

Miocene to Recent calcareous nannofossil biostratigraphy in the eastern Bengal Fan (Indian Ocean): Linking turbidites to tectonic activity during the evolution of the Himalayas

Jarrett W. Cruz*, Sherwood W. Wise Jr., William C. Parker

Department of Earth, Ocean and Atmospheric Sciences, Florida State University, Tallahassee, FL 32306, USA; Jwc09e@my.fsu.edu

Manuscript received 21st April, 2020; revised manuscript accepted 25th April, 2021

Abstract The geological history of the Himalayas and the Tibetan Plateau is currently being investigated by a broad spectrum of researchers. This paper presents the biostratigraphy of calcareous nannofossils from IODP Expedition 354, Site 1451 in the Bengal Fan. Detailed nannofossil distribution data from the Holocene (0 Ma) to the Miocene/Oligocene boundary (23 Ma) were recorded from Site 1451. Here, we utilised their biostratigraphic ages to analyse events captured in the cores that could be linked to the evolution of the Himalayas. The Gradstein et al. (2012) *Geologic Time Scale* was used to assign ages to the Martini (1971) and Okada & Bukry (1980) biozone markers. Fifty-six biostratigraphic events were observed in Site 1451, based on the distribution of 45 marker species, and these were used to interpret 51 biozones/subzones. A total of 245.1 m of turbiditic sediments were cored, from 16 to 1085.8 mbsf. This accounted for 35.9% of the total drilled sediment. The lowermost turbidite sequence was assigned an age range of 15.8 to 17.95 Ma. This study delineated at least seven pulses of turbiditic activity in this region. Two significant pulses were correlated with climatic and tectonic forcing, which are discussed as plausible source mechanisms.

Keywords nannofossils, Himalayas, Indian Ocean, evolution, turbidites, tectonics, climate forcing

1. Introduction

The Himalayas are home to some of the highest mountains in the world, with Mount Everest, located in Nepal/Tibet, being the highest mountain above sea level. The building of the Himalayas had direct effects on climatic forcing, playing a role in the evolution of the local palaeoenvironment. The geological history of this area would be expected to contain evidence of such things as monsoon winds, glacial and interglacial cycles, increased sedimentary erosion and shifting drainage systems facilitating sediment transport. While the Himalayas have attracted a great deal of investigation, a problem resides in the broadness of the evidence and in how that evidence is interpreted. Works done by authors such as Zhisheng et al. (2001), Royden et al. (2008), Wang et al. (2012) and Curray (2014) have given us a timeline for this evolution.

The evolution of the drainage systems transporting materials from the continental Himalayas to the surrounding ocean is reflected in the sediment record, providing evidence of periods when intense sedimentation took place, with the location of deposition reflecting the activity of the various drainage systems. Allen (2005), Clift & Blusztajn (2005), Curray (2014) and Blum et al. (2018) have discussed aspects of Himalayan deposition, looking into the evolution and reorganisation of the Himalayan and Tibetan river systems. These sedimentary records can

be analysed to create a source-to-sink model that can be linked to tectonic and climatic events.

Despite the rigour of these prior works, the timing of the tectonic and climatic forcing events have not always been well constrained. Our interest in the Himalayas and Tibetan Plateau was focused on the depositional characteristics of the Bengal Fan (Indian Ocean), with the goal of using calcareous nannofossils to develop a local biostratigraphic zonation scheme for a portion of this. We found strong autogenic signalling from the sediments originating in the Himalayas and Tibetan Plateau. The timing of these events can be used to test various hypotheses constructed to constrain the timing of the evolution of the Himalayas.

2. Location and methods

IODP Site 1451 was drilled in the Indian Ocean, in the eastern portion of the head of the Bengal Fan, at 8°0.4203'N, 88°44.4745'E (Figure 1). The water depth was around 3607 m to the sea floor. Hole 1451A was drilled from the sea floor to 578.5 mbsf. There was 86% recovery in the cored intervals, resulting in 497.51 m of sediment in total. Hole 1451B was drilled from 542 to 1181.3 mbsf, with 29% of the cored interval being recovered, giving a total of 185.4 m. There was a 35-m overlap between the base of Hole A and the top of Hole B. The lithology was variable throughout the cores. All the lithological units below 700

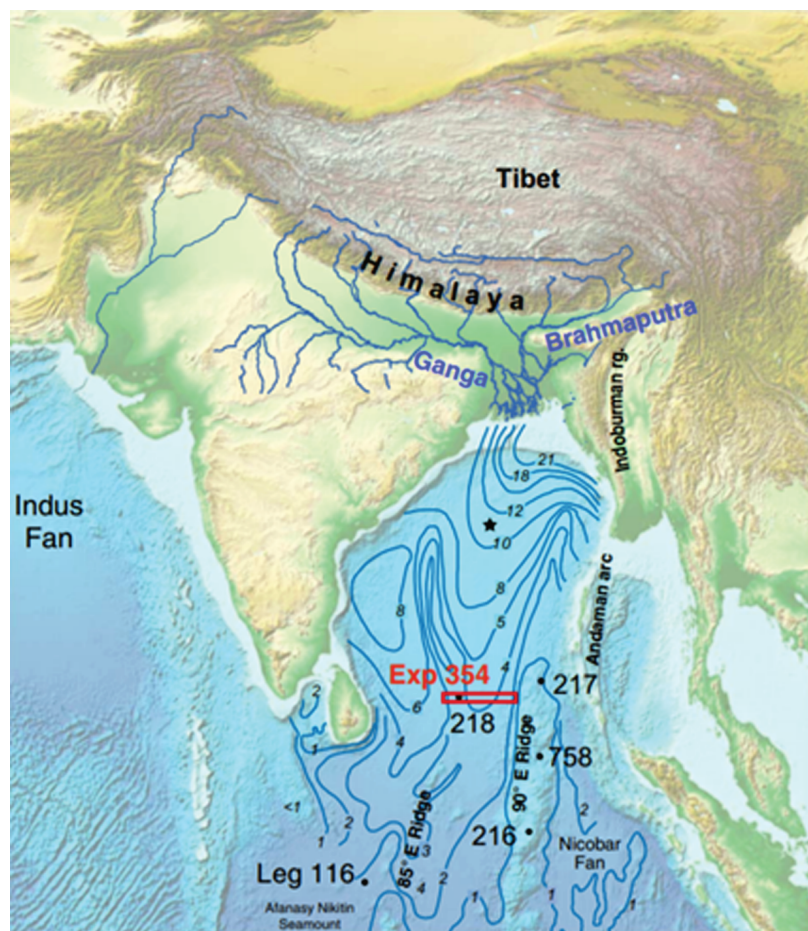


Figure 1: Location of IODP Site 1451, Indian Ocean. After France-Lanord et al. (2016)

mbsf were lithified.

Samples (20 cm^3) were collected from each 1.5-m section of the cores and vacuum-sealed in bags. High-resolution sampling (one sample per 10 mm) was performed upon visual observation of a change in lithology, and samples were taken from above, below and within turbidite units. High-resolution samples were also taken from the pelagic lithologies. A total of 420 samples were collected and examined for nannofossils. The standard smear-slide technique was used for sample preparation (Bown & Young, 1998).

The slides were examined using Zeiss Standard 25 and Zeiss Axiostar Plus light-microscopes. Counts were obtained from one traverse, viewing the samples at 1000x magnification (~ 120 fields of view). This allowed for a semiquantitative count of the species abundances. To find rare specimens, another three traverses were observed. BugWin counting software (BugWare, Inc., Tallahassee, FL, USA) was used on all 420 samples in order to compile distribution data that was then plotted for detailed analysis

and comparison using BugCad software (BugWare, Inc.).

The standard nannofossil biozonations of Martini (1971), Bukry (1973) and Okada & Bukry (1980) were used to determine the nannofossil age datums. In addition, Young (1998) and Denne et al. (2005) were employed to assign ages to the secondary events. BugWin and Nannoware software, and the Nannotax website (www.nannotax.org), were consulted to help identify the nannofossil species.

3. Biostratigraphy of Site 1451

Sixty-five global and regionally recognised nannofossil marker species, from Martini (1971), Bukry (1973), Okada & Bukry (1980), Young (1998) and Denne et al. (2005), were used to determine the biostratigraphy of Site 1451, with 61 bioevents used to assign biozones and subzones (Table 1, Plates 1–5).

An age/depth analysis of the new data from the post-cruise samples showed significant differences from the

shipboard study. The new model (Figure 2) is included here to provide a basic idea of the age/depth model for IODP Expedition 354, Site 1451. Figure 2 was created using the new biostratigraphic datapoints, along with data from Blum et al. (2018). It also shows the core recovery from the two holes from Expedition 354 and the lithological units they were assigned to.

4. Turbidite activity at Site 1451

During the expedition, as drilling was taking place and the cores were being processed, a team of sedimentologists analysed the cores, detailing the lithological variations and the presence of turbidite units. There were 245.1

Table 1 (right): Nannofossil biostratigraphy of IODP Expedition 354, Site 1451. Zones based on marker events assigned by Martini (1971, NP/NN nomenclature), in addition to Bukry (1973) and Okada & Bukry (1980, CP/CN nomenclature). Ages were calibrated based on Gradstein et al. (2012), plus one age from Young (1998) and six from Denne et al. (2005)

Depth (m)	Samples IODP core ID	Zone Martini (1971)	Zone Okada & Bukry (1980)	Age Gradstein et al. (2012) (Ma)	Markers Top/Base/X
3.67	A-1H-3, 66–67	NN21	CN15	Recent	<i>E. huxleyi</i>
29.6	A-5H-1W, 74–75	NN21/NN20	CN14b/CN15	0.29	<i>Gephyrocapsa</i> spp. and absence of <i>E. huxleyi</i>
64.38	A-11F-3W, 108–109	NN20/NN19	CN14a/CN14b	0.44	Top <i>P. lacunosa</i>
104	A-20F-1, 142–143	NN19	CN13b	1.26	Top <i>H. sellii</i>
106.2	A-20F-3, 64–65	NN19	CN13b	1.6	Top <i>C. macintyreii</i>
110.1	A-21F-2, 131–132	NN19/NN18	CN12d/CN13a	1.93	Top <i>D. brouweri</i>
122.5	A-23G-1, 100–101	NN18	CN12d	1.95	Top <i>D. triradiatus</i>
123.6	A-23H-2, 67–68	NN18/NN17	CN12c/CN12d	2.39	Top <i>D. pentaradiatus</i>
137.3	A-24H-5, 125–126	NN17/NN16	CN12b/CN12c	2.49	Top <i>D. surculus</i>
142.6	A-25H-2, 63–64	NN16	CN12a/CN12b	2.8	Top <i>D. tamalis</i> (first common)
144.3	A-25H-3, 78–79	NN16	CN12a	3.54	Top <i>Sphenolithus</i> spp. (first common)
148.2	A-25H-6, 22–23	NN16/NN15	CN11b/CN12a	3.7	<i>R. pseudoumbilicus</i>
151.8	A-26H-2, 41–42	NN15/NN14	CN11b	3.92	<i>A. tricorniculatus</i>
152.6	A-26H-3, 65–66	NN14/NN13	CN11a/CN11b	4.13	Base common <i>D.</i> <i>asymmetricus</i>
153.9	A-26H-4, 84–85	NN13	CN10c/ CN11a	4.5	<i>A. primus</i>
161.2	A-27H-2, 44–45	NN13	CN10c	5.04	Top <i>C. acutus</i>
162.7	A-27H-3, 55–56	NN13/NN12	CN10b/CN10c	5.12	Base <i>C. rugosus</i>
165	A-27H-5, 29–30	NN12	CN10b	5.28	Top <i>T. rugosus</i>
169.6	A-28H-1, 60–61	NN12	CN10a/ CN10b	5.35	Base <i>C. acutus</i>
171.1	A-28H-2, 60–61	NN12/NN11	CN9d/CN10a	5.59	Top <i>D. quinquerramus</i>
174.1	A-28H-4, 60–61	NN11		5.59 (Young, 1998)	Top <i>C. mediaperforatus</i>
183	A-29H-5, 32–33	NN11	CN9c/CN9d	5.94	Top <i>N. amplificus</i>
189	A-30H-2, 60–61	NN11		6.1 (Denne et al., 2005)	Top <i>R. rotaria</i>
255.3	A-43F-1, 80–81	NN11	CN9c	6.79	X <i>N. amplificus</i> to <i>T.</i> <i>rugosus</i>
259.1	A-43F-4, 45–46	NN11	CN9b/CN9c	6.91	Base of <i>N. amplificus</i>
301	A-52F-3, 78–79	NN11	CN9a/CN9b	7.42	Base <i>A. primus</i> /spp.
345.8	A-62F-1, 59–60	NN11	CN9a	7.53	Top <i>D. loeblichii</i>
346.4	A-62F-2, 15–16	NN11/NN10	CN8/CN9a	8.29	Base <i>D. berggrenii</i> Top <i>D. prepentaradiatus</i>
373.4	A-70F-1, 65–66	NN10	CN8	8.68	Top <i>M. convallis</i>
440.6	A-82F-1, 86–87	NN10	CN8	8.77	Base <i>D. loeblichii</i>
441.6	A-82F-2, 19–20	NN10	CN8	9.21	Top <i>D. bollii</i>
442.5	A-82F-3, 11–12	NN10/NN9	CN7/CN8	9.53	Top <i>D. hamatus</i>
449.7	A-86F-1, 65–66	NN9	CN7	9.69	Top <i>C. coalitus</i>
584.95	B-6X-4, 56–57	NN9/NN8	CN6/CN7	10.55	Base <i>D. hamatus</i>
590.9	B-6X-6, 27–28	NN8	CN6	10.76	Base <i>D. brouweri</i>
620.2	B-11X-1, 60–61	NN8/NN7	CN5b/CN6	10.89	Base <i>C. coalitus</i>
695.14	B-20R-1, 61–62	NN7	CN5b	11.21	Top <i>C. premacintyreii</i>
717.54	B-22R-3, 2829	NN7	CN5b	11.85	Top <i>C. floridanus</i>
787.96	B-29R-4, 58–59	NN7/NN6	CN5a/CN5b	11.9	Base common <i>D.</i> <i>kugleri</i>
794.53	B-30R-2, 84–85	NN6	CN5a	12.12	Top <i>C. nitescens</i>
831.41	B-34R-1, 44–45	NN6	CN5a	12.83	Base <i>R.</i> <i>pseudoumbilicus</i>
831.41	B-34R-1, 44–45	NN6	CN5a	13.1 (Denne et al., 2005)	Top <i>D. virginianus</i>
845	B-36R-1, 35–36	NN6	CN5a	13.28	Top common <i>C.</i> <i>floridanus</i>
872.3	B-38R-2, 119–120	NN6/NN5	CN4/CN5a	13.53	Top <i>S. heteromorphus</i>
899.61	B-41R-1, 51–52	NN5	CN4	14.1 (Denne et al., 2005)	Top <i>D. petaliformis</i>
948.88	B-46R-1, 108–109	NN5/NN4	CN3/CN4	14.91	Top <i>H. ampliaptera</i>
954.23	B-47R-3, 2–3	NN4	CN3	15.8	Abundant <i>D. deflandrei</i> group
1096.93	B-63R-3, 33–34	NN4/NN3	CN2/CN3	17.95	Top <i>S. belemnus</i>
1098.35	B-63R-4, 81–82	NN3/NN2	CN1c/CN2	18.28	Top <i>T. carinatus</i>
1114.75	B-65R-2, 40–41	NN2	CN1c	20.8 (Denne et al., 2005)	Top <i>S. dissimilis</i>
1127.61	B-67R-4, 71–72	NN2	CN1c	22.76	Base <i>S. disbelemnus</i>
1130.56	B-67R-6, 84–85	NN1	CN1a–b	23.11	Top <i>S. delphix</i>
1136	B-68R-4, 0–0	NN1/NP25	CP19b/CN1a–b	23.13	Top <i>R. bisecta</i>

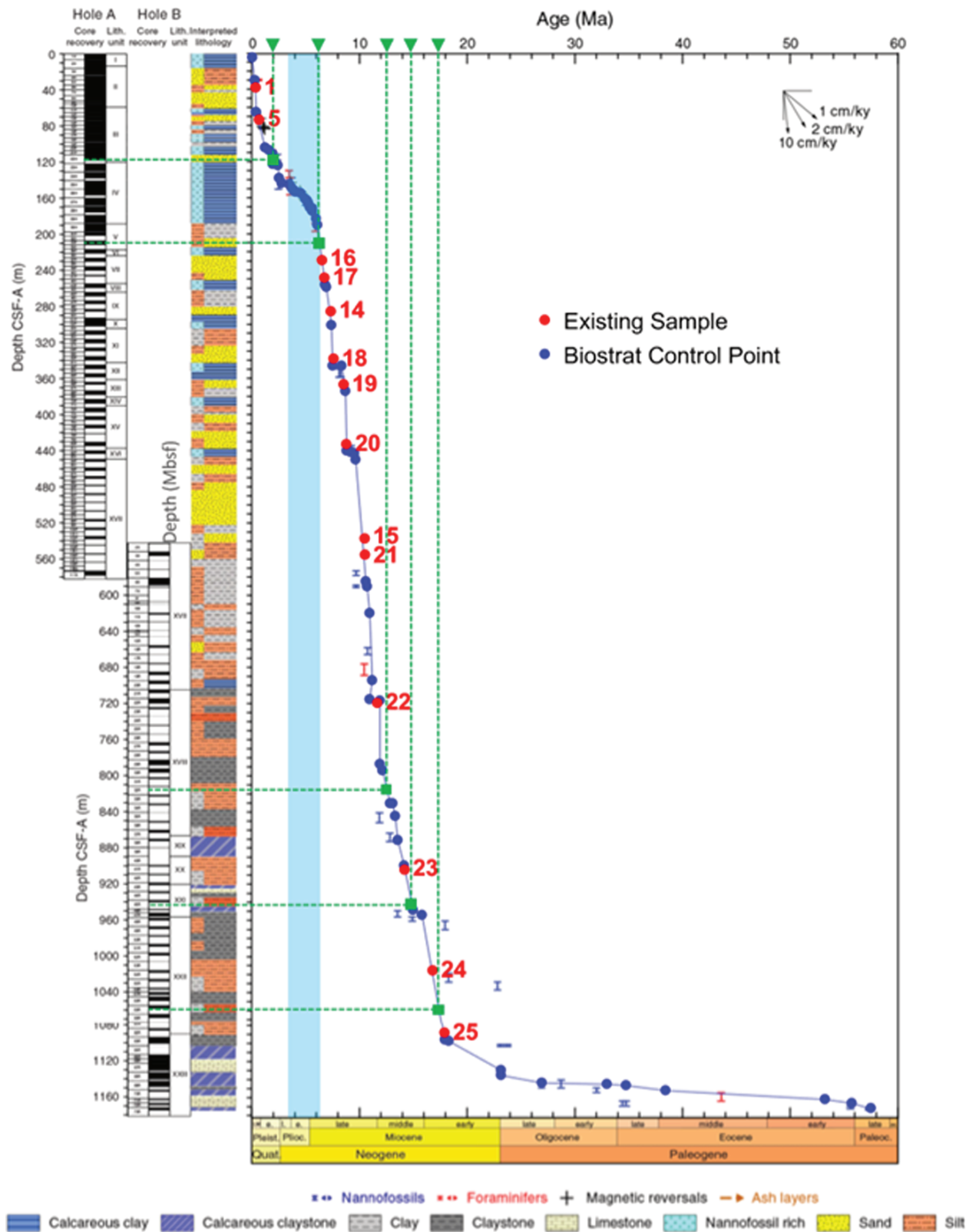


Figure 2: Age/depth plot for IODP Site 1451, including data from Blum et al. (2018) and the new nannofossil datapoints (this study, in blue). The red datapoints are foraminiferal age constraints and the green datapoints are radiometric age constraints (after Blum et al., 2018). The lithological units are those interpreted during the expedition

m of core listed as silt, sand or turbidite, accounting for 35.9% of the total recovered sediment. From these descriptions, we listed the identified turbidite units (Table 2). We assigned ages to each unit based on the nannofossil markers identified from above, below and within the units. Reworked Palaeogene nannofossils were consistently observed; however, we had high confidence in the biostratigraphy due to the Neogene marker-species present in the pelagic and hemipelagic sediments.

An important goal for Site 1451 was to identify the lowermost turbidite unit; the lowest sequence was observed in Core 62R, its base being at 1085.8 m. An age of 15.8 to 17.95 Ma was assigned to the unit. Based on sedimentological observations and nannofossil ages, there appeared to be at least seven pulses of turbidite activity present in the cores.

The turbidite units were produced by turbidity currents, which are a form of sediment gravity flow where sediment grain support is generated by turbulence. The stronger the turbidity flow, the larger the grain size of the sediments it can carry. Coarser sediment grains are carried in the bed near the front of the flow. These currents are responsible for creating canyons, channels and lobes in the world's oceans. When a turbidity current deposits turbidite units, it usually follows the Bouma sequence of lithologies. Coarser materials are deposited at the base, with the grain size grading to finer particles towards the top in a layer-stacking event that is usually repeated, sequence upon sequence. Layers can be lost or compressed due to mixing or settling.

In the observed turbiditic units, seven events were identified when split by nannofossil zone. An Early Miocene event was recorded between Cores 354-1451B-49R and 354-1451B-62R (967.27–1086.47 m). There were 9.2 m of turbiditic lithology recorded. This event was in NN4 (17.95–15.8 Ma) and represented the earliest recorded turbidite at Site 1451.

The second oldest event was during the Middle Miocene, recorded between Cores 354-1451B-41R and 354-1451B-45R (899.1–940.44 m). There were 7.49 m of turbiditic section in NN5 (~15.8–14.1 Ma). The third event was in 354-1451B-29R to 354-1451B-37R (785.91–863.31 m), where 13.99 m of turbidites were observed in NN6 (~13.53–11.9 Ma). The fourth event was recorded in 351-1451B-13X to 354-1451B-29R (639–785.86 m). Here, there were 20.7 m of turbiditic section in the NN7/

NN8 transition and NN7 (~11.85–10.89 Ma).

The other three events occurred in Upper Miocene sediments, the fifth recorded between 351-1451A-84F and 354-1451B-6X (449.3–581.72 m), totalling 29.06 m. This event was in NN9 (10.55–9.69 Ma). In NN7–9 (10.97–9.69 Ma), there were 36.46 m of turbidites, averaging 28.07 m/Myr—almost double the average depositional rate at the site (i.e. 14.58 m/Myr). The sixth event was in 354-1451A-66F to 354-1451A-82F (363.7–441.2 m), with 24.52 m of turbidites in the NN10/NN11 transition and NN10 (9.21–8.29 Ma). The seventh event was recorded between 351-1451A-28H and 354-1451A-60F (174.45–339.99 m). There were 59.44 m of turbidites, falling in NN11 (~8.29–5.59 Ma). From 8.29–6.1 Ma, there were 58.14 m of turbidite sediments reported. This was 26.55 m/Myr, also nearly double the recorded average (i.e. 14.58 m/Myr).

5. Discussion

5.1 Early Miocene uplift of the Tibetan Plateau and the initiation of monsoons

The Early Miocene evolution of the Himalayas and the Tibetan region saw a major shift in the palaeoenvironment. This is thought to be the timing of the initiation of monsoons in the region as a result of significant tectonic forcing. The Early Miocene was characterised by long-term sea-level highstands and the Early to Middle Miocene Climatic Optimum (Betzler et al., 2018). This coincided with crustal thickening and rapid surface uplift in the Tibetan Plateau. There was active eastward flow of deep crust, while southward thrusting was taking place in the Lesser Himalayas (Royden et al., 2008). This significant tectonic activity, coupled with the onset of monsoons, thought to have initiated around 20–15 Ma (Clift et al., 2008), generated copious amounts of clastic material, which was transported south into the Bay of Bengal. This correlates with the initiation of turbidite deposition at Site 1451. In NN4, between 17.95 and 15.8 Ma, 9.2 m of turbidites were preserved in Cores 354-1451B-49R to 354-1451B-62R (967.27–1086.47 m), and these contained significant plant-fragment inclusions; in fact, 13.7 m of sediments containing plant-fragment inclusions were recorded from Site 1451 in this time interval (Cruz, 2020).

Around 20–15 Ma, rapid erosion and transport of sediment from the Himalayas (Clift et al., 2008; Blum et al., 2018) resulted in deposition in the Bay of Bengal via the

Core	Start depth (m)	End depth (m)	Martini (1971) Zone	GTS2012 Age (Ma)	Turbidite units	Core	Start depth (m)	End depth (m)	Martini (1971) Zone	GTS2012 Age (Ma)	Turbidite units
				Recent		354-U1451A-84F	449.3	452.11	NN9	9.53/9.69	5
354-U1451A-3H	16	23.62	NN21	age		354-U1451A-86F	458.7	462.09			
354-U1451A-4H	24	25.23				354-U1451A-88F	468.26	469.29			
	25.77	27					469.6	471.11			
	27.44	28.93									
354-U1451A-5H	28.9	29.56	NN21/NN20	0.29		354-U1451A-90F	477.7	479.19			
						354-U1451A-92F	487.2	489.01			
	29.73	29.89	NN20			354-U1451A-94F	496.7	497.76			
	30.4	34.75				354-U1451A-96F	506.2	507.55			
354-U1451A-6H	34.75	39.75				354-U1451A-98F	515.7	518.38			
354-U1451A-7H	39.7	42.96				354-U1451A-102F	534.7	537.91			
	42.96	46.33				354-U1451A-104F	544.2	545.18			
354-U1451A-8H	46.3	52.38				354-U1451A-106F	553.7	555			
354-U1451A-9H	52.3	55.56				354-U1451A-111X	576.12	576.54			
354-U1451A-10H	55.6	60.74			354-1451B-3X	551.82	556.27				
			354-1451B-4X	561.4	561.68						
			354-1451B-5X	571.1	571.6						
			354-1451B-6X	580.93	581.72				NN9/NN8	10.55	
354-U1451A-12H	67.74	69.76	NN19					NN8	10.76		
354-U1451A-13H	69.7	74.3									
354-U1451A-14H	74.4	79.39			354-1451B-10X	610	610.1				
354-U1451A-16F	83.92	85.19								NN8/NN7	10.89
	85.42	85.47			354-1451B-13X	639	639.29	NN7	11.21	4	
	85.64	85.68			354-1451B-16R	655.6	658.27				
	85.7	86.7			354-1451B-18R	675.2	676.3				
354-U1451A-17F	88.58	88.68			354-1451B-19R	685	687.63				
	92.48	93.45				687.66	687.92				
354-U1451A-19F	97.9	102.85				688.09	688.44				
					NN19/NN18	1.93	354-1451B-20R				694.8
354-U1451A-22H	112	118.37	NN18		696.69	696.88					
			NN12/NN11	5.59	697.2	697.27					
					697.35	697.43					
354-U1451A-28H	174.45	174.62	NN11	5.94 6.1	7		697.72				697.86
	174.82	174.89				354-1451B-21R	704.78	705.33			
	175.3	175.89					705.6	705.68			
354-U1451A-29H	180.84	181.31					705.68	705.8			
							705.89	706.1			
						354-1451B-22R	714.4	717.25			
354-U1451A-30H	189.86	191.36									11.85
	191.67	197.19				354-1451B-24R	734	734.19	NN6	12.12	3
354-U1451A-31F	197.5	198.88				354-1451B-27R	763.2	766.42			
	199	201.63				354-1451B-28R	772.8	775.15			
354-U1451A-31H	197.5	198.81				354-1451B-29R	782.5	784.26			
354-U1451A-33F	207	211.79					784.94	785.86			
354-U1451A-37F	226	230.65					785.91	787.43			
354-U1451A-39F	235.5	240.34									
354-U1451A-41F	245	246.64		788.1	788.51	NN6	12.12	3			
354-U1451A-45F	264	268.99	354-1451B-30R	792.23	795.19						
354-U1451A-47F	273.5	277.37		795.19	796.75						
354-U1451A-49F	283	285.68	354-1451B-32R	811.6	812.55						
			354-1451B-33R	821.3	823.12						
			354-1451B-34R	831	832.73						
354-U1451A-54F	306.7	311.51								12.83-13.1	
354-U1451A-56F	316.2	321.03								13.28	
354-U1451A-58F	325.7	329.61									
354-U1451A-60F	335.2	339.99	NN11/NN10	8.29		354-1451B-37R	860.27	863.31	NN6/NN5	13.53	
354-U1451A-66F	363.7	366.76	NN10	8.68	6	354-1451B-41R	899.1	900.77	NN5	14.1	2
						354-1451B-42R	908.9	910.32			
354-U1451A-68F	374.7	375.69				354-1451B-43R	918.6	920.56			
354-U1451A-70F	384.61	385.16				354-1451B-45R	938	940.44			
354-U1451A-72F	392.23	397.11							NN5/NN4	14.91	
354-U1451A-74F	401.7	405.94								15.8	
354-U1451A-76F	411.2	415.08				354-1451B-49R	967.27	970.13	NN4		1
354-U1451A-78F	420.7	421.63				354-1451B-52R	996.4	997.25			
354-U1451A-80F	430.2	434.77					998.06	999.34			
354-U1451A-82F	439.78	441.2				354-1451B-53R	1006.16	1006.31			
			NN10/NN9	9.53	354-1451B-54R	1015.8	1016.17				
						1016.4	1018.26				
					354-1451B-55R	1025.6	1028.29				
					354-1451B-56R	1035.3	1037.2				
					354-1451B-59R	1054.8	1058.4				
					354-1451B-61R	1074.2	1074.8				
					354-1451B-62R	1083.9	1086.47				
										17.95	

Table 2: Turbiditic sequences found during IODP Expedition 354, Site 1451

Ganges River system. By 18 Ma, the drainage of Tibet via the Ganges was at least partially integrated with that of the Brahmaputra River, and significant uplift in the Tibetan region would have caused an increase in sediment transport through the Brahmaputra River system into the Bengal Fan.

5.2 Middle Miocene climatic forcing

The early Middle Miocene includes the Middle Miocene Cooling Event, a time when palaeotemperatures indicate a significant drop in temperature coincident with a long-term sea-level lowstand. The eastern Antarctic ice-sheet expanded, causing this decrease in sea level, at around 15.1 Ma (Betzler et al., 2018), and this climatic driver likely contributed to the increased deposition of turbidites at Site 1451. This increase was recorded between Cores 354-1451B-41R and 354-1451B-45R (899.1–940.44 m), with 7.49 m of turbidites occurring in NN5 (15.8–14.1 Ma). There was also a shift in plant-fragment deposition during this interval. At around 14.91 to 14.1 Ma, there were 3.08 m of plant-fragment inclusions in the turbidite deposits. However, before that, from 15.8–14.91 Ma, there was no turbidite deposition. Platform growth in the Maldives at this time saw a shift from aggradation to progradation, as noted by Betzler et al. (2018), while at Site 1451, there was a shift from turbidite deposition to 30 m of pelagic/hemipelagic deposition (i.e. lasting for 890 kyr).

In the late Middle Miocene, the monsoon winds in the Indian Ocean strengthened (Betzler et al., 2018). At this time, there was a change in sedimentation patterns, driven by these shifting monsoon winds, as well as alterations to the circulation in the Indian Ocean. The hypothesised timing of this strengthening coincided with two significant pulses in turbidite deposition and an increase in plant-fragment inclusions. The first of these pulses was found in Cores 354-1451B-29R to 354-1451B-37R (785.91–863.31 m), with 13.99 m of turbidites dated as NN6 (13.53–11.9 Ma). The second was recorded between 351-1451B-13X and 354-1451B-29R (639–785.86 m), with 20.7 m of turbidites dated as NN7/NN8 and NN7 (11.85–10.89 Ma). Betzler et al. (2018) determined an increase in organic-matter content in deposits lying above the shift in depositional patterns. This can be seen at Site 1451, between 11.9 and 10.89 Ma, where there were 10.22 m of section containing plant-fragment inclusions, compared to 2.27 m from 12.83 to 11.9 Ma. This increase in deposition and

plant fragment inclusion supports a strengthening of the monsoon winds, as hypothesised by Betzler et al. (2018).

5.3 Late Miocene tectonic and climatic forcing

Wang et al. (2012) suggested that the Himalayas underwent tectonic forcing around 7+ Ma, uplifting the region by 2–2.5 km to its current elevation of 4100–4500 masl. This timing of central Himalayan uplift is supported by the increase in turbidite deposition at Site 1451 between cores 351-1451A-28H and 354-1451A-60F (174.45–339.99 m), where 59.44 m of turbidites were deposited, which account for 24.25% of the total turbidite deposition at the site. This depositional event is in NN11, and occurred from 8.29 to 5.59 Ma. There was a significant pulse around 7.42–6.1 Ma, demarcated by the top occurrence of *Reticulofenestra rotaria* and the base occurrence of *Amaurolithus primus*. Of the 157.4 m of sediments deposited in this interval, 55.08 m were turbidites. The sedimentation rate during this time was high, at 26.55 m/Myr.

Wang et al. (2012) showed a similar increase in sedimentation rate, to 60 ± 22 mm/kyr, in the Gyirong Basin (Tibet), where sediment accumulated between 10.2 and 7.2 Ma. Simultaneously (8.29–6.1 Ma), transported sedimentation increased at Site 1451. This supports significant uplift occurring in the central Himalayas around 7.42+ Ma.

Two other events occurred during the Late Miocene that can be attributed to climatic forcing in eastern Tibet. Zhishent et al.'s (2001) hypothesis that enhanced aridity in the Asian interior, along with the onset of strengthening in the Indian monsoon, was initiated around 9–8 Ma is supported by the increase in sedimentation rates during this period. This would have increased erosion and the transport of materials from the continental shelf into the Bay of Bengal. The first event was recorded between 351-1451A-84F and 354-1451B-6X (449.3–581.72 m). The 29.06 m of turbiditic section (11.85% of the total turbidite deposition at site 1451) occurred in NN9 and around the NN9/NN8 boundary (~10.55–9.69 Ma). From 10.97–9.69 Ma, there were 36.46 m of turbidite sediments, with a relatively high sedimentation rate of 28.07 m/Myr. This pulse in turbidite deposition supports the hypothesis (Zhishent et al., 2001) that further significant uplift in this region may have occurred around 10–8 Ma. The second event was recorded between 354-1451A-66F and 354-1451A-82F (363.7–441.2 m). The 24.52 m of turbidites lie within

the NN11/NN10 transition and NN10, at around 9.21–8.29 Ma. This accounted for 10% of the total turbidite deposition at Site 1451.

6. Conclusions

Biostratigraphy is a critical tool for investigating the evolutionary history of a region. In addition to providing a timeframe for the turbiditic events at Site 1451, the nanofossil dates were used in testing a number of hypotheses from a broad array of studies. Wang et al. (2012) suggested that a major tectonic event occurred in the Himalayan region ~7.2 Ma, which created a palaeolake basin. The current study indicated that an uplift event was initiated around 7.42⁺ Ma in the central Himalayas. An et al. (2001) hypothesised uplift in the Tibetan Plateau around 10–8 Ma. The current study inferred such an event to have occurred around 9.69⁺ Ma. Betzler et al. (2018) indicated that a monsoon-wind-driven model was influencing sedimentation patterns around 17–15.1 Ma. The current study supported a strong climatic event occurring around 15.8–14.91 Ma. Clift et al. (2005) and Royden et al. (2008) both hypothesised an Early Miocene evolution of the Himalayas and Tibetan Plateau. At this time, around 17.95–15.8 Ma, Site 1451 had just begun receiving turbidite deposits, confirming that the evolution of the Himalayas was well underway in the Early Miocene. These correlations prove that high-resolution nanofossil biostratigraphic data are key to providing a chronostratigraphic framework for the evolution of the Himalayas.

By understanding the timing of turbidite deposition, these sediments can be linked to the forcing mechanisms behind their formation. By doing this, an understanding of the regional and global processes that took place during the evolution of the Himalayas and Tibetan Plateau can be obtained. Early Miocene tectonic forcing triggered the initiation of turbidite deposition at Site 1451. This tectonic activity likely impacted the Middle Miocene climatic forcing that increased turbidite deposition here. During the Late Miocene, tectonic and climatic forcing increased, again altering the intensity and frequency of turbidite deposition in the Bay of Bengal. This framework provides a backdrop for future studies, while showcasing how critical calcareous nanofossil biostratigraphy can be in furthering our understanding of the evolution of the Himalayas, and also in providing a high-resolution age model for addressing other issues in the Cenozoic history of the Indian

Ocean.

Acknowledgements

This work could not have been done without: samples and funding from the IODP and help from the scientists who sailed on Expedition 354; the geology programme in the Department of Earth, Ocean and Atmospheric Science at FSU; and BugWare, Inc. for supplying us with BugWin and BugCad. We would also like to thank Drs David Bord, Richard Howe and Jackie Lees for the time and effort they put into reviewing this article. All supplementary materials can be found in Cruz, Jarrett W. 2020. *Utilizing Indian Ocean calcareous nanofossil biostratigraphy of Miocene sediments to investigate tectonic and climatic forcing during the evolution of the Himalayas*. Florida State University, ProQuest Dissertations Publishing. 27999239. <https://search.proquest.com/openview/8b28b39dd5eb015c7d03ffee4da7afd3/1?pq-origsite=gscholar&cbl=18750&diss=y>

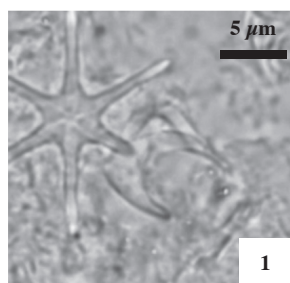
References

- Allen, P.A. 2005. Volte-face in the Punjab. *Nature*, **438**: 925–926.
- An, Z., Kutzbach, J.E., Prell, W.L. & Porters, S.C. 2001. Evolution of Asian monsoons and phased uplift of the Himalayan–Tibetan plateau since Late Miocene times. *Nature*, **411**: 62–66.
- Betzler, C., Eberli, G.P., Lüdmann, T., Reolid, J., Kroon, D., Reijmer, J.J.G., Swart, P.K., Wright, J., Young, J.R., Alvarez-Zarikian, C., Alonso-García, M., Bialik, O.M., Blättler, C.L., Guo, J.A., Haffen, S., Horozal, S., Inoue, M., Jovane, L., Lanci, L., Laya, J.C., Hui Mee, A.L., Nakakuni, M., Nath, B.N., Niino, K., Petruny, L.M., Pratiwi, S.D., Slagle, A.L., Sloss, C.R., Su, X. & Yao, Z. 2018. Refinement of Miocene sea level and monsoon events from the sedimentary archive of the Maldives (Indian Ocean). *Progress in Earth and Planetary Science*, **5**(1): 1–18.
- Blum, M., Rogers, K., Gleason, J., Najman, Y., Cruz, J. & Fox, L. 2018. Allogenic and autogenic signals in the stratigraphic record of the deep-sea Bengal Fan. *Nature Scientific Reports*, **8**(7973).
- Bown, P.R. & Young, J.R. 1998. Techniques. In: P.R. Bown (Ed.). *Calcareous nanofossil biostratigraphy*. British Micropalaeontological Society Publications Series/Chapman & Hall, London: 16–21.
- Bukry, D. 1973. Coccolith stratigraphy, eastern equatorial Pacific, Leg 16 Deep Sea Drilling Project. *Initial Reports of the DSDP*, **16**: 653–711.
- Clift, P.D. & Blusztajn, J. 2005. Reorganization of the western

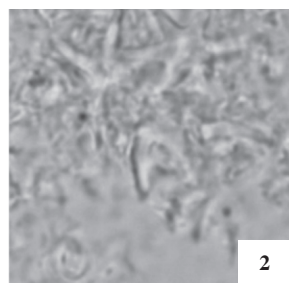
- Himalayan river system after five million years ago. *Nature*, **438**: 1001–1003.
- Clift, P.D., Clark, M.K. & Royden, L.H. 2008. An erosional record of the Tibetan Plateau uplift and monsoon strengthening in the Asian marginal seas. Archived 27 May 2008 at the Wayback Machine. Retrieved 11 May 2008.
- Cruz, J.W. 2020. *Utilizing Indian Ocean calcareous nannofossil biostratigraphy of Miocene sediments to investigate tectonic and climatic forcing during the evolution of the Himalayas*. PhD dissertation, Florida State University.
- Curry, R.J. 2014. The Bengal depositional system: From rift to orogeny. *Marine Geology*, **352**: 59–69.
- Denne, R., Callender, A. & Nault, M. 2005. *Applied Biostratigraphic Gulf of Mexico biostratigraphic chart*. Neogene calcareous nannofossils, Houston TX, **1**: 1–3.
- France-Lanord, C., Spiess, V., Klaus, A., Adhikari, R.R., Adhikari, S.K., Bahk, J.-J., Baxter, A.T., Cruz, J.W., Das, S.K., Dekens, P., Duleba, W., Fox, L.R., Galy, A., Galy, V., Ge, J., Gleason, J.D., Gyawali, B.R., Huyghe, P., Jia, G., Lantzsich, H., Manoj, M.C., Martos Martin, Y., Meynadier, L., Najman, Y.M.R., Nakajima, A., Ponton, C., Reilly, B.T., Rogers, K.G., Savian, J.F., Schwenk, T., Selkin, P.A., Weber, M.E., Williams, T. & Yoshida, K. 2016. Site U1450. Proceedings IODP, 354. doi:10.14379.iodp.proc.354.104.2016
- Gradstein, F.M., Ogg, J.G., Schmitz, M.D. & Ogg, G.M. 2012. *A Geologic Time Scale 2012*. Cambridge University Press: 1138–1149.
- Martini, E. 1971. Standard Tertiary and Quaternary calcareous nannoplankton zonation. *Proceedings of the II Planktonic Conference, Roma, Tecnoscienza*, **2**: 739–785.
- Okada, H. & Bukry, D. 1980. Supplementary modification and introduction of code numbers to the low-latitude coccolith biostratigraphic zonation (Bukry, 1973; 1975). *Marine Micropaleontology*, **5**: 321–325.
- Royden, L.H., Burchfiel, B.C. & van der Hilst, R.D. 2008. The Geological Evolution of the Tibetan Plateau. *Science*, **321**: 1054–1058.
- Wang, Y., Deng, T., Flynn, L.J., Wang, X., Yin, A., Xu, Y., Parker, W.C., Lochner, E., Zhang, C. & Biasatti, D. 2012. Late Neogene environmental changes in the central Himalaya related to tectonic uplift and orbital forcing. *Journal of Asian Earth Sciences*, **44**: 62–76.
- Young, J.R. 1998. Neogene. In: P.R. Bown (Ed.). *Calcareous nannofossil biostratigraphy*. British Micropalaeontological Society Publications Series/Chapman & Hall, London: 225–265.
- Zhisheng, A., Kutzbach, J.E., Prell, W.L. & Porters, S.C. 2001. Evolution of Asian monsoons and phased uplift of the Himalayan–Tibetan Plateau since Late Miocene times. *Nature*, **411**: 62–66.

Plate 1

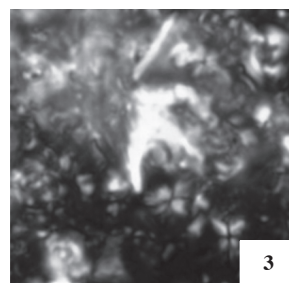
Amaurolithus, *Calcidiscus*, *Catinaster*, *Ceratolithus*



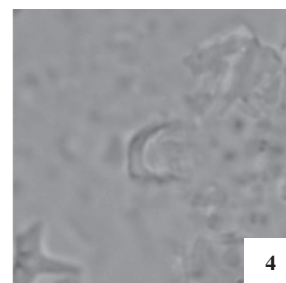
Amaurolithus primus



A. primus



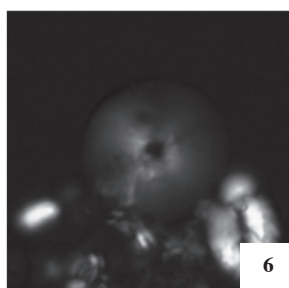
A. primus



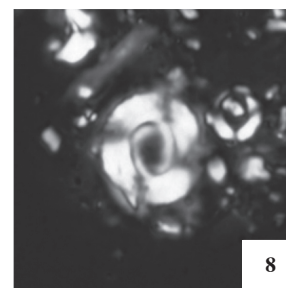
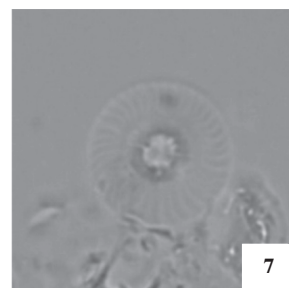
A. tricorniculatus



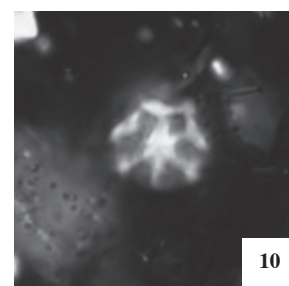
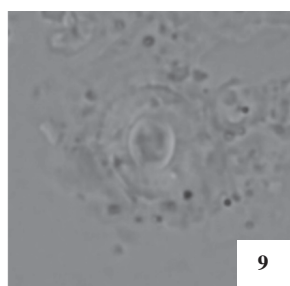
A. tricorniculatus



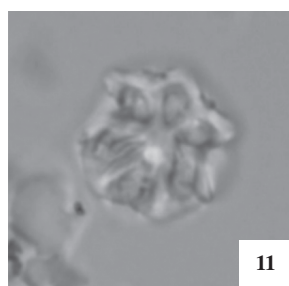
Calcidiscus macintyreii



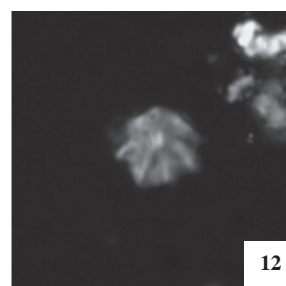
C. premacintyreii



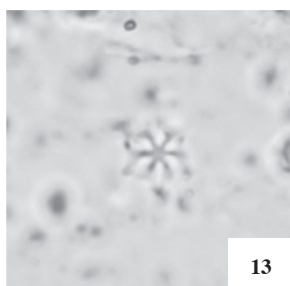
Catinaster coalitus



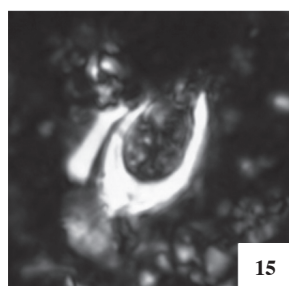
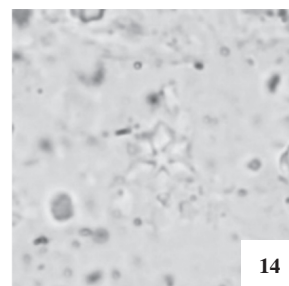
C. coalitus



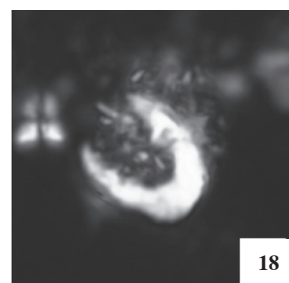
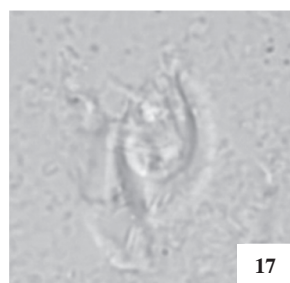
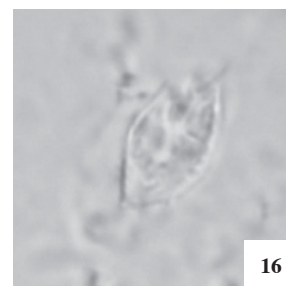
C. sp. A. (Discoaster virginianus)



C. sp. A. (Discoaster virginianus)



Ceratolithus acutus



Ceratolithus rugosus

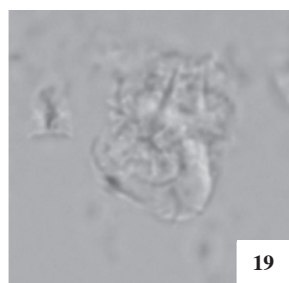
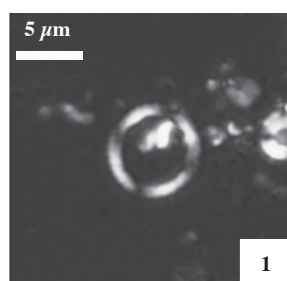
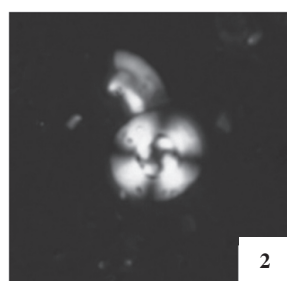


Plate 2

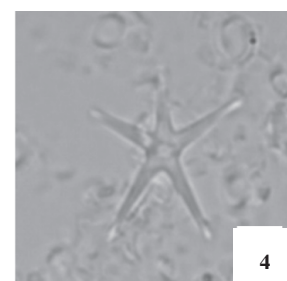
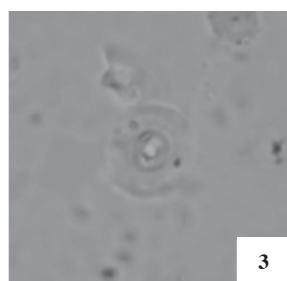
Coronacyclus, Cyclicargolithus, Discoaster



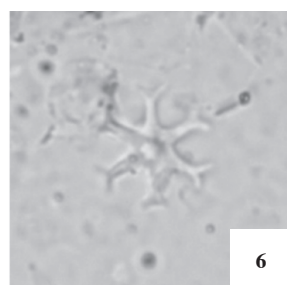
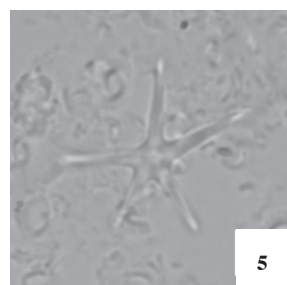
Coronacyclus nitescens



Cyclicargolithus floridanus



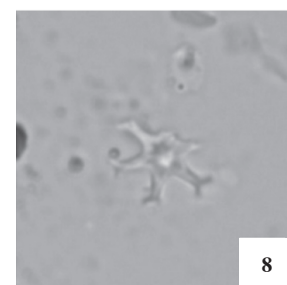
Discoaster asymmetricus



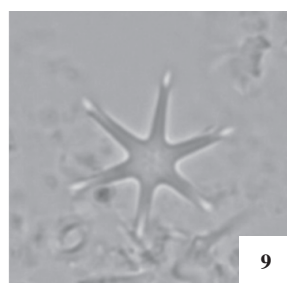
D. bollii



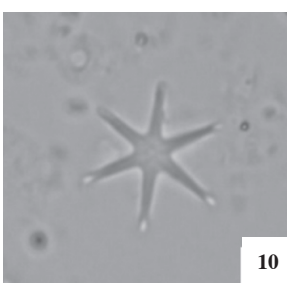
D. bollii



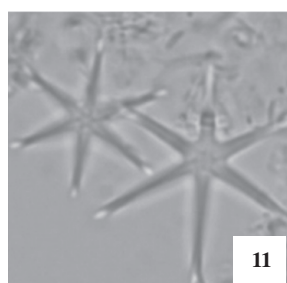
D. bollii



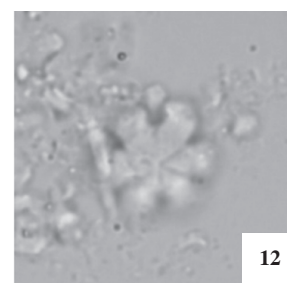
D. brouweri



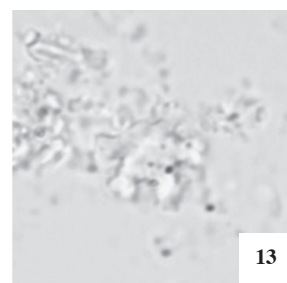
D. brouweri



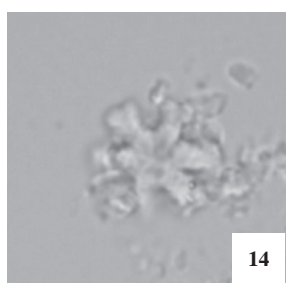
D. brouweri



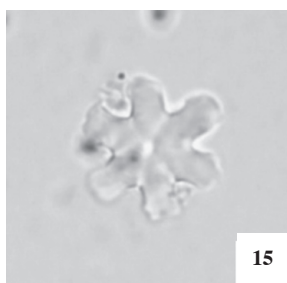
D. deflandrei



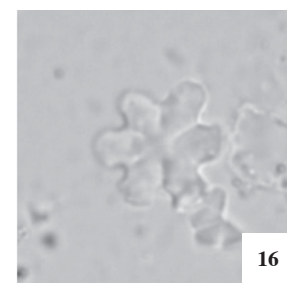
D. deflandrei



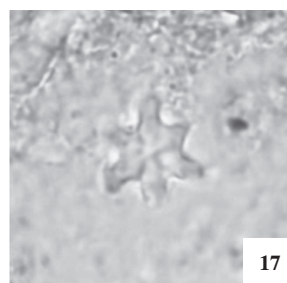
D. deflandrei



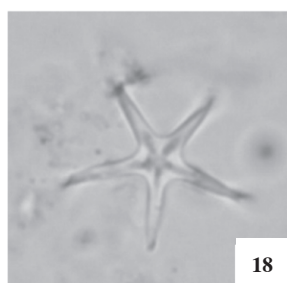
D. druggii



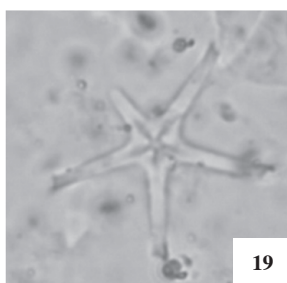
D. druggii



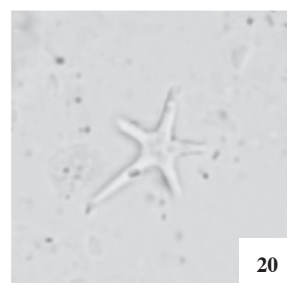
D. druggii



D. hamatus



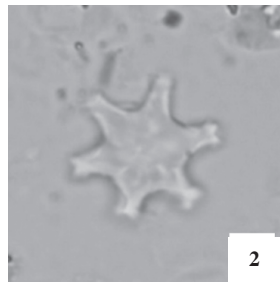
D. hamatus



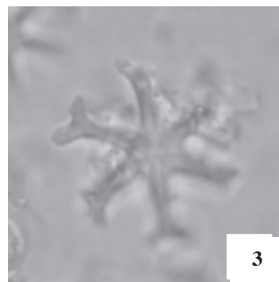
D. hamatus

Plate 3

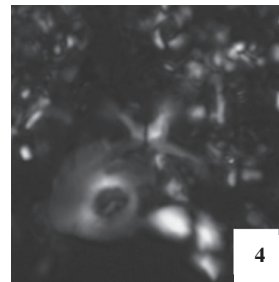
Discoaster

*Discoaster kugleri*

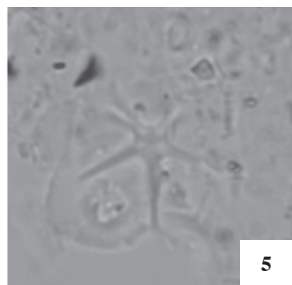
2



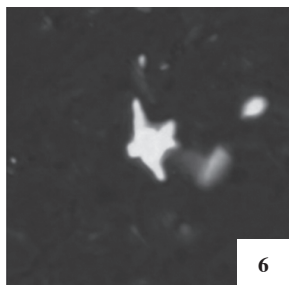
3

D. loeblichii

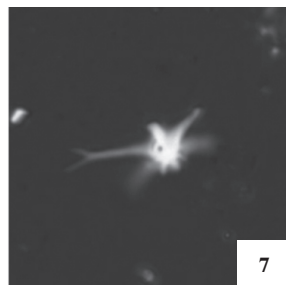
4

D. pentaradiatus

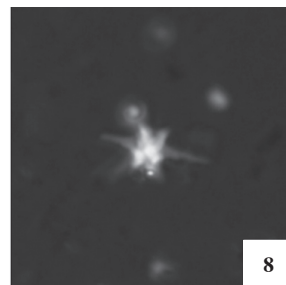
5



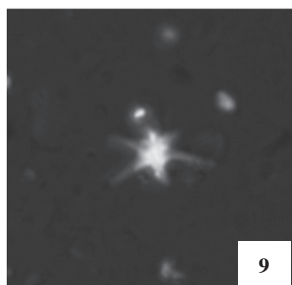
6

D. petaliformis

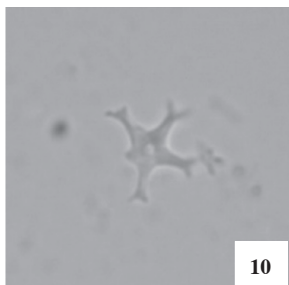
7

D. petaliformis

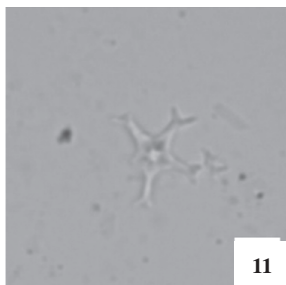
8

D. petaliformis

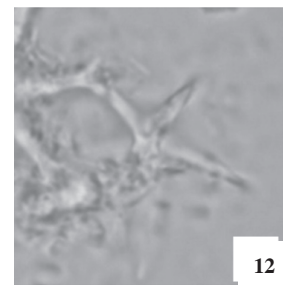
9



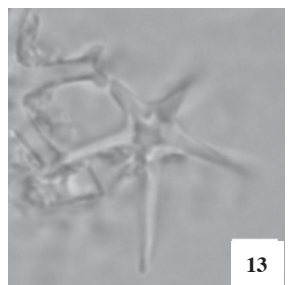
10

D. prepentaradiatus

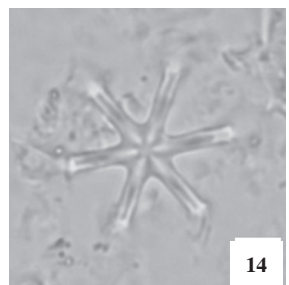
11



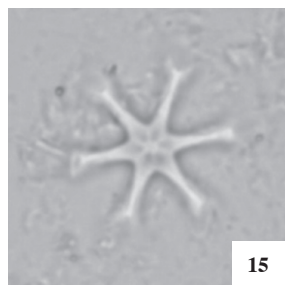
12

D. quinquaradiatus

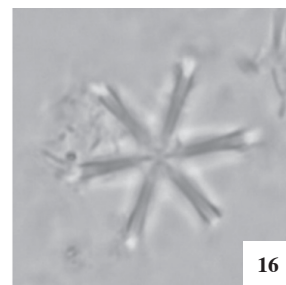
13

D. quinquaradiatus

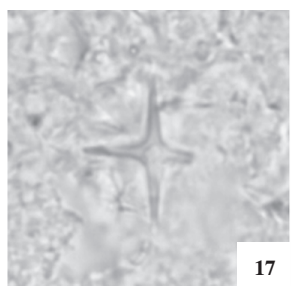
14

D. surculus

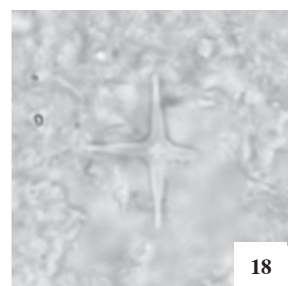
15



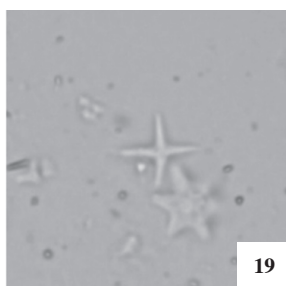
16



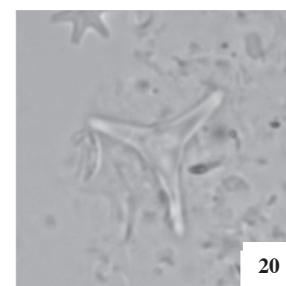
17

D. tamalis

18



19

D. tamalis

20

D. triradiatus

Plate 4

Discoaster, *Gephyrocapsa*, *Helicosphaera*, *Minylitha*, *Nicklithus*

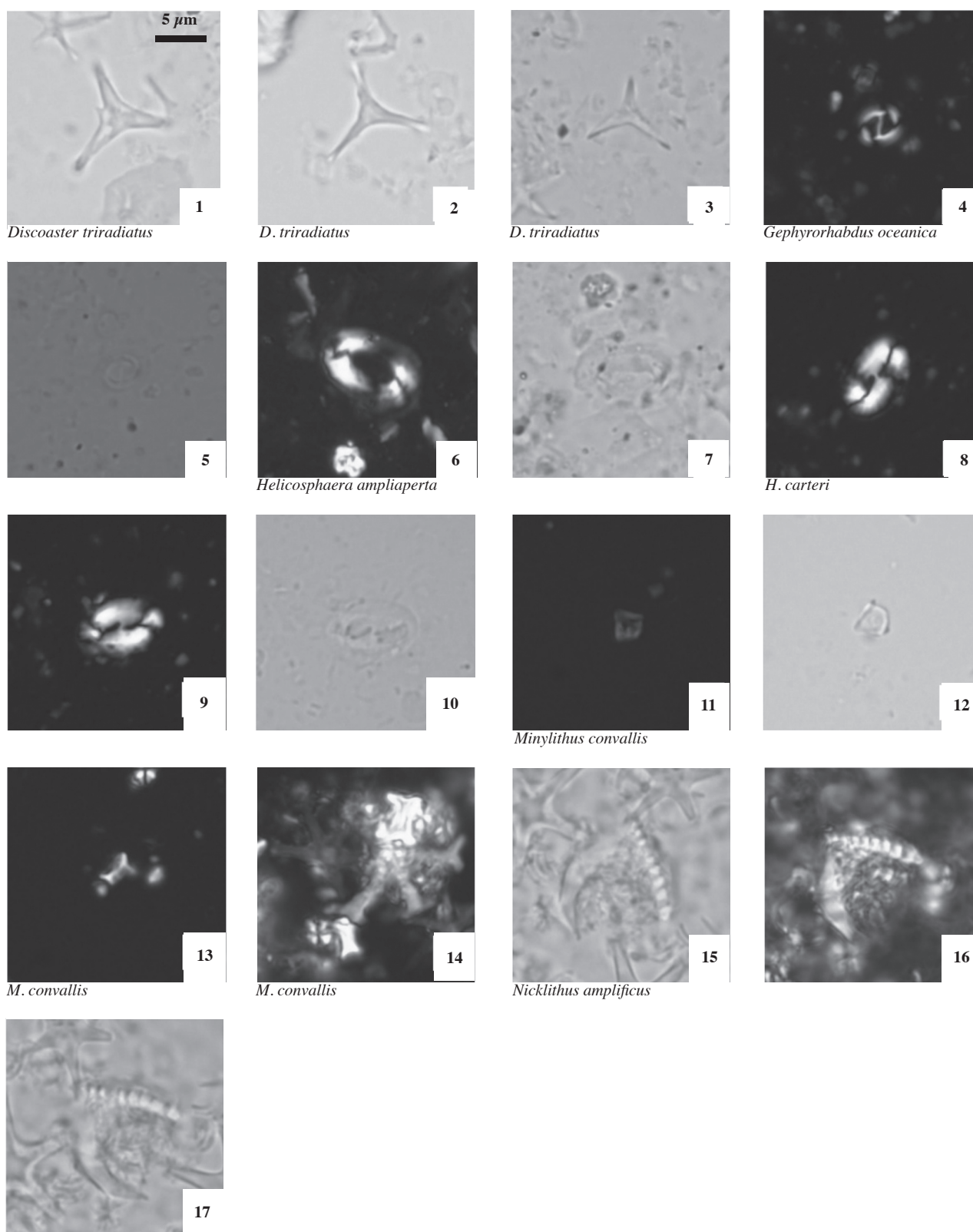
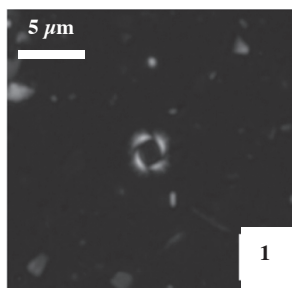
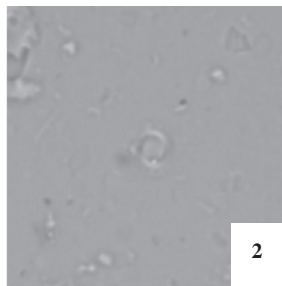


Plate 5

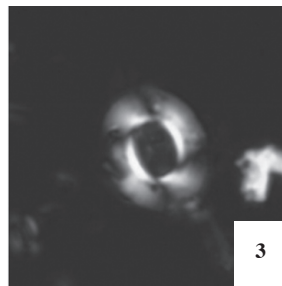
Pseudoemiliana, *Reticulofenestra*, *Sphenolithus*, *Triquetrorhabdulus*



Pseudoemiliana lacunosa

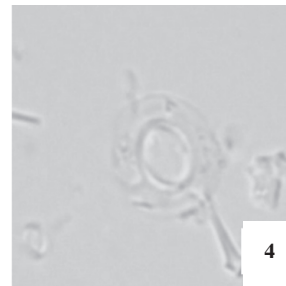


2

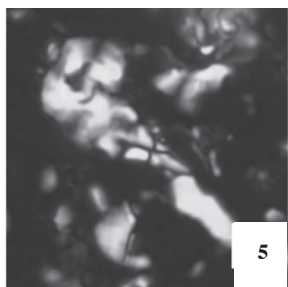


3

Reticulofenestra pseudumbilicus

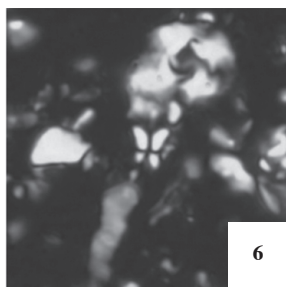


4

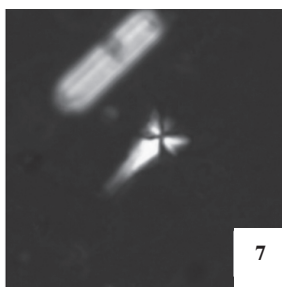


5

Sphenolithus belemnus

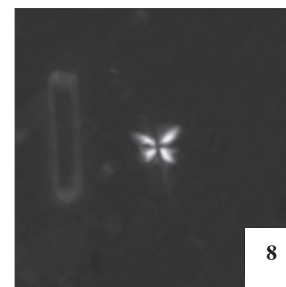


6



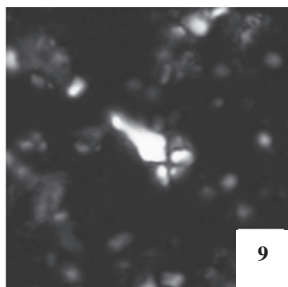
7

S. heteromorphus



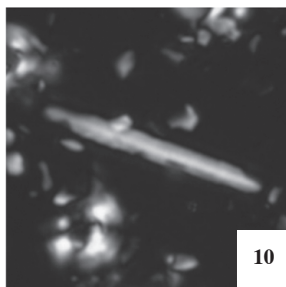
8

S. heteromorphus



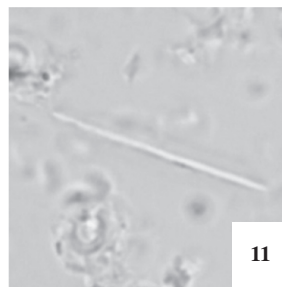
9

S. heteromorphus

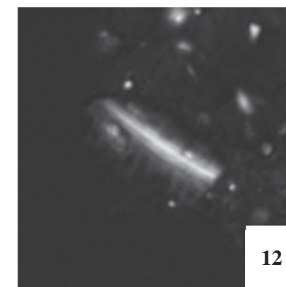


10

Triquetrorhabdulus carinatus

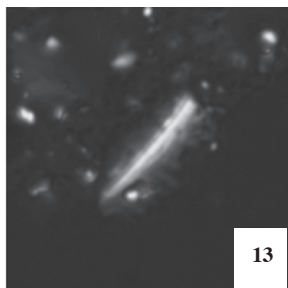


11



12

T. rugosus



13